


Article

Synthesis, Characterization, and Photocatalytic Activity of Ba-Doped BiFeO₃ Thin Films

Khiat Abdelmadjid ¹, Felicia Gheorghiu ^{2,*}  and Boughelout Abderrahmane ¹

¹ Research Center in Industrial Technologies (CRTI), P.O. Box 64 Cheraga, Algiers 16014, Algeria; khiatmadjid2018@gmail.com (K.A.); abderrahmanebugh@gmail.com (B.A.)

² RAMTECH, Department of Exact and Natural Sciences, Institute of Interdisciplinary Research, Alexandru Ioan Cuza University of Iasi, Blvd. Carol I, nr. 11, 700506 Iasi, Romania

* Correspondence: felicia.gheorghiu@uaic.ro

Abstract: In the present paper, Bi_{1-x}Ba_xFeO₃ (BBFO) thin films (where x = 0, 0.02 and 0.05) were prepared by a combined sol-gel and spin-coating method. The influence of Ba substitutions on the structural, microstructural, optical properties, and photocatalytic activity of BiFeO₃ thin films has been studied. X-ray diffraction pattern correlated with FTIR analysis results confirms that all the films have a perovskite structure of rhombohedral symmetry with an R3m space group. Atomic force microscopy (AFM) and scanning electron microscopy (SEM) were used to investigate the surface morphology and reveals microstructural modifications with the increase in Ba concentration. The optical properties show that the band gap is narrowed after doping with Ba ions and decreases gradually with the increase of doping content. The photocatalytic investigations of deposited films revealed that Ba doping of BFO material leads to the enhancement of photocatalytic response. The present data demonstrates that Bi_{1-x}Ba_xFeO₃ (BBFO) thin films can be used in photocatalytic applications.

Keywords: perovskites; films; optical properties; doped BaTiO₃; photocatalytic activity



Citation: Abdelmadjid, K.; Gheorghiu, F.; Abderrahmane, B. Synthesis, Characterization, and Photocatalytic Activity of Ba-Doped BiFeO₃ Thin Films. *Materials* **2022**, *15*, 961. <https://doi.org/10.3390/ma15030961>

Academic Editor: John T. Kiwi

Received: 4 January 2022

Accepted: 24 January 2022

Published: 26 January 2022

Publisher's Note: MDPI stays neutral with regard to jurisdictional claims in published maps and institutional affiliations.



Copyright: © 2022 by the authors. Licensee MDPI, Basel, Switzerland. This article is an open access article distributed under the terms and conditions of the Creative Commons Attribution (CC BY) license (<https://creativecommons.org/licenses/by/4.0/>).

1. Introduction

Today, evolution of modern society leads to a continuous increasing of environmental pollution. Therefore, degradation of organic pollutants shows a great interest for photocatalytic applications [1]. To date, several semiconductors can act as photocatalysts: TiO₂, ZnO, Fe₂O₃, CdS, ZnS [2–6]. TiO₂ is the most studied photocatalysts [2,7,8], but the wide band gap (3.2 eV) [8] provides low efficiency of absorption in the visible-light region. This problem leads to the searching for new oxide-based photocatalysts with strong absorbance for visible-light applications. Semiconductor-based photocatalysts are promising materials for degradation of a large number of organic contaminants.

In the last years, the multiferroic materials have become an attractive research area due its interest in photocatalytic field [9,10]. The advantage of multiferroics in comparison with usual photocatalysts is their low band gap energy. Among multiferroic materials, perovskite BiFeO₃ (BFO) is one of the few and best known room—temperature multiferroics, that has a distorted perovskite structure that belongs to rhombohedral R3c symmetry (with $a = 3.958$ and $\alpha = 89.30^\circ$), with a high ferroelectric Curie temperature ($T_C = 830$ °C) and antiferromagnetic order ($T_N = 370$ °C) [11–13]. The preparations of BiFeO₃ powder material were reported by different synthesis methods, as for example: solid-state reaction method [14], hydrothermal synthesis route [15], sol-gel process [16] combustion method [17], Pechini method [18], and microwave synthesis [19]. However, the preparation of BiFeO₃ is very difficult due to: (i) The kinetics of phase formation in the Bi₂O₃-Fe₂O₃ system that leads to the formation of impurities along with the perovskite major phase [20] and thermal stability; (ii) valence fluctuation of iron (Fe³⁺/Fe²⁺ transitions) which leads to the variation of oxygen stoichiometry and appearance of the oxygen vacancies as defects; (iii) Bi volatilization because bismuth oxide has a low melting point. Therefore, in spite of

different preparation methods, the powdered photocatalysts presents some disadvantages in comparison with thin films: difficulty in particle separation, a high cost, agglomeration effect at high concentration [21]. Consequently, BiFeO₃ thin films have drawn considerable interest due to its potential to be used as photocatalytic films.

In order to overcome the problems and limitations regarding the obtaining of BiFeO₃ powder system, a strategy was adopted of using various dopants substitution on Bi sites as Ca, Sr, Ba, Nd, Sm, La [22–25]. In the present case, Ba²⁺ ion as dopant in BFO was chosen, as its ionic radius (1.35 Å) is higher than that of Bi³⁺ ion (1.03 Å) and can compensate the Fe-O-Fe exchanges. By Ba ion substitution on Bi sites, it is also expected that the surface area will increase and improve the photocatalytic activities by decreasing the band gap energy. In the literature Ba-doped BiFeO₃ material as nanoparticles [26], nanofibers [27], ceramics [28], and even as thin films was reported [29,30]. However, there are no reports focused on the Ba-doped BiFeO₃ thin films as photocatalysts.

In the present paper, Bi_{1-x}Ba_xFeO₃ (BBFO) thin films (where x = 0, 0.02 and 0.05) were prepared by a combined sol-gel and spin-coating method. The influence of Ba substitution on the structural (using XRD analysis), morphology (by SEM and AFM investigations), and narrowing of the band gap energy was investigated and the obtained results are discussed in detail. The main goal of the present paper is the photocatalytic activity investigations, data that were not reported until this moment for Bi_{1-x}Ba_xFeO₃ as thin films. The photocatalytic activity of BBFO thin films was investigated by the degradation of Rhodamine B (RhB) under solar light irradiation. Rhodamine B was chosen as the organic pollutant for this study because it is reported in the literature with high degradation efficiency [21]. Ba influences on the photocatalytic properties will be also discussed.

2. Preparation and Experimental Details

BBFO thin films were synthesized on glass substrates by using sol-gel-assisted spin-coating technique, according to the preparation scheme represented in the Figure 1. Bismuth nitrate pentahydrate (Bi(NO₃)₃·5H₂O, Sigma-Aldrich, Saint Louis, MO, USA), iron nitrate nonahydrate (Fe(NO₃)₃·9H₂O, Sigma-Aldrich, Saint Louis, MO, USA), and barium acetate ((CH₃COO)₂Ba, 99%, Sigma-Aldrich, Darmstadt, Germany) were used as the starting precursors and were dissolved in ethylene glycol as solvent in order to obtain a final precursor solution of 0.2 M concentration.

The chosen Ba dopant concentration in BBFO thin films are as follows: x = 0, x = 0.02 and x = 0.05. In order to prevent and compensate for a possible volatilization of Bi during post deposition annealing processes, 10% excess bismuth nitrate was added. The resulted solutions were mixed together and then stirred for 1 h at 80 °C in order to get a well-mixed BBFO gel solution.

Then a few drops of acetic acid were added to the BBFO solution as a stabilizer. Afterwards, this mixed solution was spin-coated onto ultra-cleaned glass substrate, while spinning at a high speed of 3000 rpm for 40 s to obtain uniform films. After spinning, a drying treatment of 320 °C for 5 min is applied for removing the remaining solvent. The spin-coating and drying treatment processes are repeated twice. At the end, the films were transferred to the furnace and annealed at 500 °C for 4 h in ambient atmosphere to consolidate the films by a complete crystallization.

The phase formation of the BBFO thin films after the thermal treatment step were checked at room temperature with PANalytical Empyrean X-ray (Almelo, The Netherlands) diffractometer using CuK α radiation ($\lambda = 1.5406$ Å) and operating in the 2θ range of 20–60°, with a step size of $2\theta = 0.04^\circ$. The phase identification was performed using X'pert High Score software (version 4.9) supported with ICDD database. The phase formation was checked also by using Fourier transform infrared (FTIR) spectra, recorded in the range 600–3000 cm⁻¹ on a Bruker Vertex 70 FTIR Spectrometer with the aim to complete the phase identification by ascribing the peaks to the various modes.

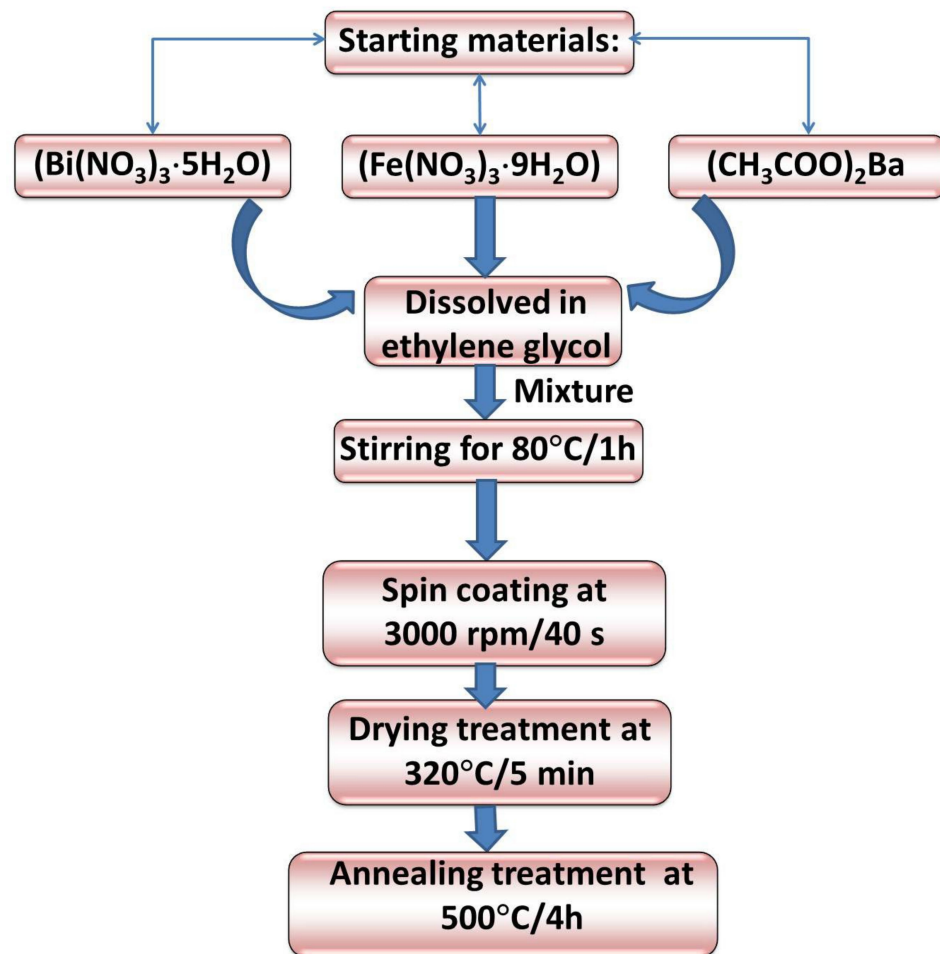


Figure 1. Preparation flowchart of $\text{Bi}_{1-x}\text{Ba}_x\text{FeO}_3$ (BBFO) thin films.

The film's surface images and morphologies were investigated by using a scanning electron microscope (SEM, type JEOL JCM-5000 Neoscope, Akishima, Tokyo, Japan) and by atomic force microscopy (AFM, type JEOL SPM5200, Tokyo, Japan). The UV-visible absorption spectra were recorded by using UV-vis spectrophotometer (Lambda 35, from Perkin Elmer, Waltham, MA, USA). The investigation of the prepared films as photocatalysts for degrading of organic RhB was carried out under natural sunlight with an irradiation power of $\sim 800 \text{ mW/cm}^2$. Day light from a September sunny day with about 25°C was used to perform the photocatalytic experiments. In order to prevent thermal effect or vaporization, the films were placed into a Pyrex reactor container. The reactor was placed for cooling into a thermostatic water bath during the measurements in order to maintain a constant temperature of 25°C . In each experiment, a solution of RhB (100 mL volume, 10 mg/L concentration) was taken for batch studies.

3. Results and Discussion

3.1. Phase, Structural, and Microstructural Characterization

The XRD pattern for $\text{Bi}_{1-x}\text{Ba}_x\text{FeO}_3$ thin films (where $x = 0, 0.02$ and 0.05) measured at room temperature is shown in Figure 2. The XRD peaks for $x = 0$ and 0.05 corresponding to the planes (010), (110), $(\bar{1}10)$, $(\bar{1}\bar{1}1)$, (020), $(\bar{1}20)$, $(\bar{2}11)$, indicates the formation of single-phase perovskite with typical rhombohedral type structure [11,21,26,29,30] with the $R3m$ space group identified with ICDS file no. 01-072-2112.

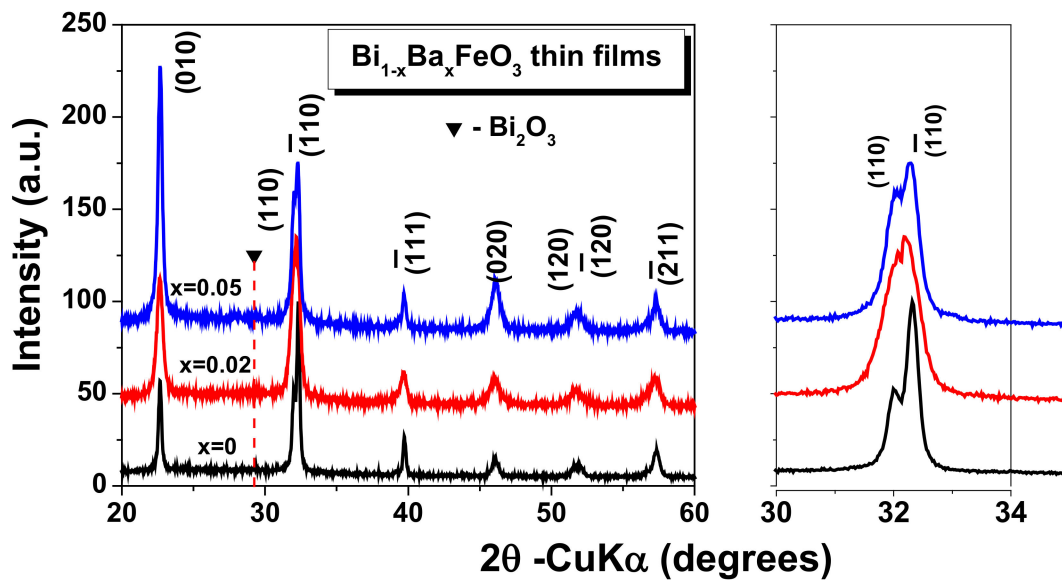


Figure 2. The XRD pattern for $\text{Bi}_{1-x}\text{Ba}_x\text{FeO}_3$ (BBFO) thin films.

The XRD patterns confirm the incorporation of Ba^{2+} ions in the BiFeO_3 lattice, with small traces of secondary phases of Bi_2O_3 . Anyway, it can be observed from enlarger view of the XRD pattern within 2θ between 30° and 34° that doping with Ba^{2+} ions induces changes in structural stability of the pure BFO. A small increase in the dopant concentration leads to a slightly shift in the principal peak position to the lower angles than of the pure BFO, which can be associated to the strain relaxation in thin films with dopant additions. Present results are in good agreement with reported data from Ref. [26]. This small shifting can be explained by taking into account the higher value of the Ba^{2+} ionic radius in comparison with that one of Bi^{3+} which distorts the original structure of pure BFO due to the internal stress induced by Ba ions in the perovskite structure of BFO. The XRD intensities peaks and full width at half maximum intensity (FWHM) positions modification are the effect of the Ba addition and can be explained by considering the contributions from both the crystallite size and the strain that may be present in the films.

In order to understand the effect of Ba doping on the phase and structural, the crystallite size and tolerance factor were calculated and analyzed and the results are summarized in the Table 1. The crystallite size of the investigated $\text{Bi}_{1-x}\text{Ba}_x\text{FeO}_3$ thin films has been calculated from XRD data using the Scherrer's formula [31] as given by the following Equation (1):

$$D = \frac{0.9\lambda}{\beta \cos \theta} \quad (1)$$

where D is the average crystallite size, 0.9 (constant) is a shape factor, $\lambda = 1.5406 \text{ \AA}$ is the wavelength of used $\text{CuK}\alpha$ radiation, β is the peak broadening at half of the maximum intensity (FWHM, in radians) after subtracting the instrumental line broadening, and θ is the diffraction Bragg angle. In comparison with pure BFO, Ba^{2+} substitutions lead to a decrease of crystallite size in BBFO thin films.

To describe the stability and structural deformation of the perovskite structure, the Goldschmidt tolerance factor was calculated after the formula given by the Equation (2):

$$t = \frac{((1-x)r_{\text{Bi}} + xr_{\text{Ba}}) + r_{\text{O}}}{\sqrt{2}(r_{\text{Fe}} + r_{\text{O}})} \quad (2)$$

where r_{Bi} , r_{Ba} , r_{Fe} , and r_{O} are the effective ionic radii of Bi^{3+} (1.03 \AA), Ba^{2+} (1.35 \AA), Fe^{3+} (0.65 \AA), and O^{2-} (1.42 \AA) ions respectively. The tolerance factor is calculated using the ionic sizes from Shannon [32]. From data reported in the Table 1, it can be observed that the

tolerance factor increases slightly but gradually with Ba^{2+} ions concentration from 0.89 for the pure BFO to 0.893 for the BBFO thin films. It is known that for the ideal cubic perovskite structures, tolerance factor is about 0.9–1 value and for distorted perovskite structure (e.g., orthorhombic/rhombohedral) the values are between 0.71 and 0.9 [33]. According to the Equation (2), the fact that Ba^{2+} ionic radius is bigger than Bi^{3+} leads to an increase in tolerance factor which is in good agreement with the calculated results. Most probably, the Ba-doped BiFeO_3 system is tending to transform from rhombohedral to a pseudo-cubic structure since the value of the tolerance factor for the highest Ba^{2+} concentration ($x = 0.05$) is tilting to 0.9 value. This also results in BFO covalent bonds changes, including bond angles like Fe-O-Fe, Bi-O-Fe, or Bi-O-Bi and bond lengths as Bi-O, Bi-Fe, Bi-Fe that took place due to the internal stresses produced by Ba substitution [30].

Table 1. Structural parameters calculated * for the $\text{Bi}_{1-x}\text{Ba}_x\text{FeO}_3$ ($0 \leq x \leq 0.05$) thin films.

Samples	Crystal Symmetry	$a(\text{\AA})$	Cell Volume $V(\text{\AA}^3)$	Crystallite Size $D(\text{nm})$	Tolerance Factor (t)
$x = 0$	Rhombohedral	3.9262	60.57	41.22	0.890
$x = 0.02$	Rhombohedral	3.9441	61.34	14.55	0.892
$x = 0.05$	Rhombohedral	3.9322	60.79	18.67	0.893

* by using the formula from Ref. [34].

To complete the structural discussion, FTIR spectroscopy was employed to study the stretching and bending vibrations of the various bonds present in the studied films. The spectra of the BBFO films (with $0 \leq x \leq 0.05$) in the IR (infrared) region were collected at room temperature in the range between 600 and 3000 cm^{-1} and are shown in the Figure 3. Since the measurements start from 600 cm^{-1} , the FTIR spectra could not confirm exactly the Fe-O stretching or O-Fe-O bending vibration modes corresponding to the 547 cm^{-1} and 435 cm^{-1} respectively [35–38]. Anyway, the absorption band traces that can be seen around 600 cm^{-1} make us to assign it to the Fe-O stretching vibrations of FeO_6 group in the perovskite compounds [35]. The obvious absorption bands near 756 cm^{-1} and $\sim 891\text{ cm}^{-1}$ can be attributed to the Bi-O bending vibration for the pure BFO film [39] and also may be due to the metal-oxygen Ba-O stretching vibration [40] for BBFO films. The band located at $\sim 2362\text{ cm}^{-1}$ most possibly indicates the presence of nitrate ions [41]. The peaks observed at ~ 2852 and 2900 cm^{-1} are assigned to C-H symmetric stretching vibrations [41]. The presence of metal-oxide bands in the measured spectrum indicates that the BBFO have crystallized in a perovskite structure for all the films. No significant peak shifting was observed due to the barium doping.

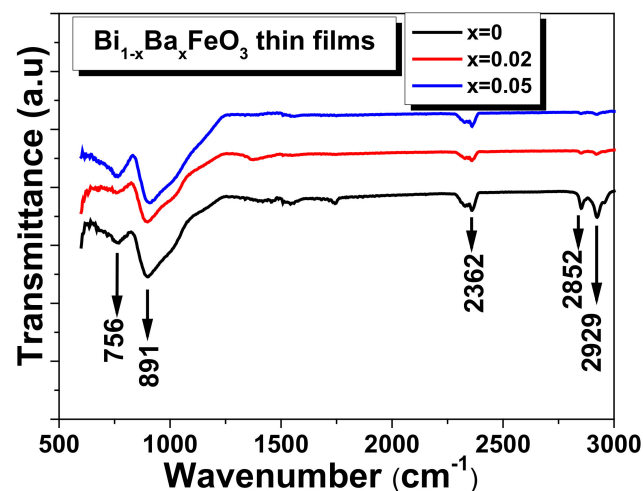


Figure 3. The room temperature FTIR spectra of $\text{Bi}_{1-x}\text{Ba}_x\text{FeO}_3$ ($0 \leq x \leq 0.05$) thin films.

The surface morphology of the studied films was investigated by using atomic force microscopy (AFM) over $5 \times 5 \mu\text{m}^2$ area in semi-contact mode. In the Figure 4 are presented the 3D topography AFM images for BBFO thin films with $x = 0, 0.02,$ and 0.05 Ba^{2+} concentrations. It can be seen that all the films have grown without any cracks but in the same time the Ba addition affects the thin films microstructure and surface morphology. As Ba^{2+} concentration level increases, the grains tend to agglomerate and form larger particles that leads to surface inhomogeneity. From AFM morphology measurements it is evidenced an increase in the surface root mean square roughness (R_{rms}) with increasing percentage of Ba^{2+} ions. The surface root mean square roughness varies from 4.9 nm to 8.9 nm and 31.8 nm , respectively for Ba^{2+} doping concentrations increasing from $x = 0$ to $x = 0.05$.

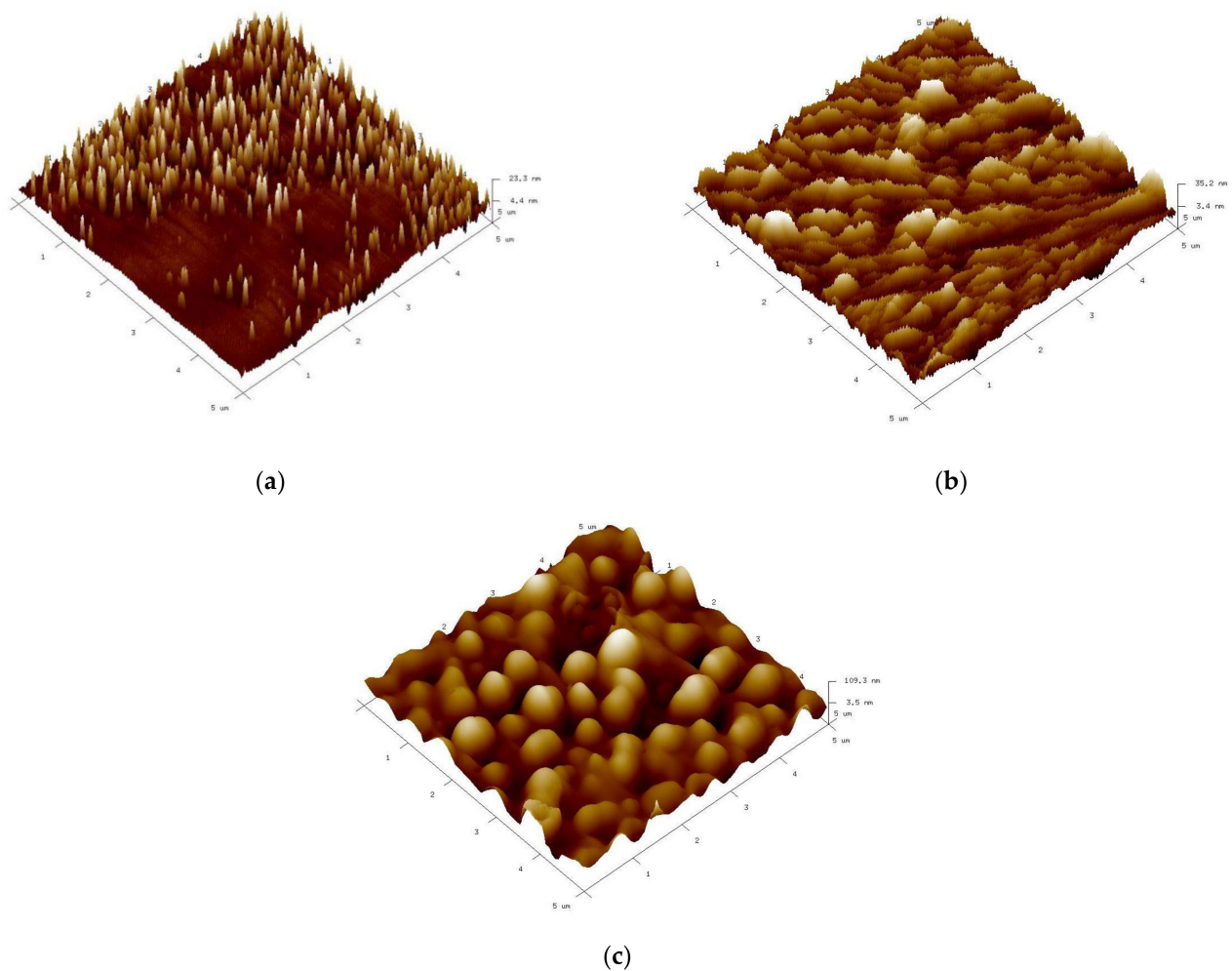


Figure 4. AFM images showing the surface topography 3D of the $\text{Bi}_{1-x}\text{Ba}_x\text{FeO}_3$ thin films for: $x = 0$ (a), $x = 0.02$ (b), and $x = 0.05$ (c).

Figure 5 shows the surface SEM images of the BBFO thin films with $x = 0, 0.02,$ and 0.05 concentrations. Since all other synthesis parameters are the same, it can be concluded that with increasing Ba^{2+} concentration, the morphology of the particle and grains changed. As shown in the Figure 5a, the pure BFO thin films present a smooth surface morphology with a small degree of porosity. With Ba doping increasing, the porosity decreases due to the grain size increasing that become irregular (as shape) for the $x = 0.05$ concentration, as it can be observed from Figure 5b,c. The average grain size of the films increases from $\sim 100 \text{ nm}$ for the pure BFO to $\sim 500 \text{ nm}$ for the Ba-doped BFO film with $x = 0.05$ concentration. Most probably, this is due to the fact that when Bi^{3+} is substituted by Ba^{2+} ions, it results in the formation of a higher number of oxygen vacancies for charge compensation and

consequently in a change of nucleation rate and growth leading to particle coarsening. The present data are not in agreement with the reported data in Ref. [30] that found a decrease in the grain sizes with an increase in Ba due to the oxygen vacancies reduction that appears as an effect of charge compensation mechanism. An increase in grain size has been reported for similar BiFeO₃ system doped with La³⁺ [41], NaNbO₃ [42] or even with Ba³⁺ [43].

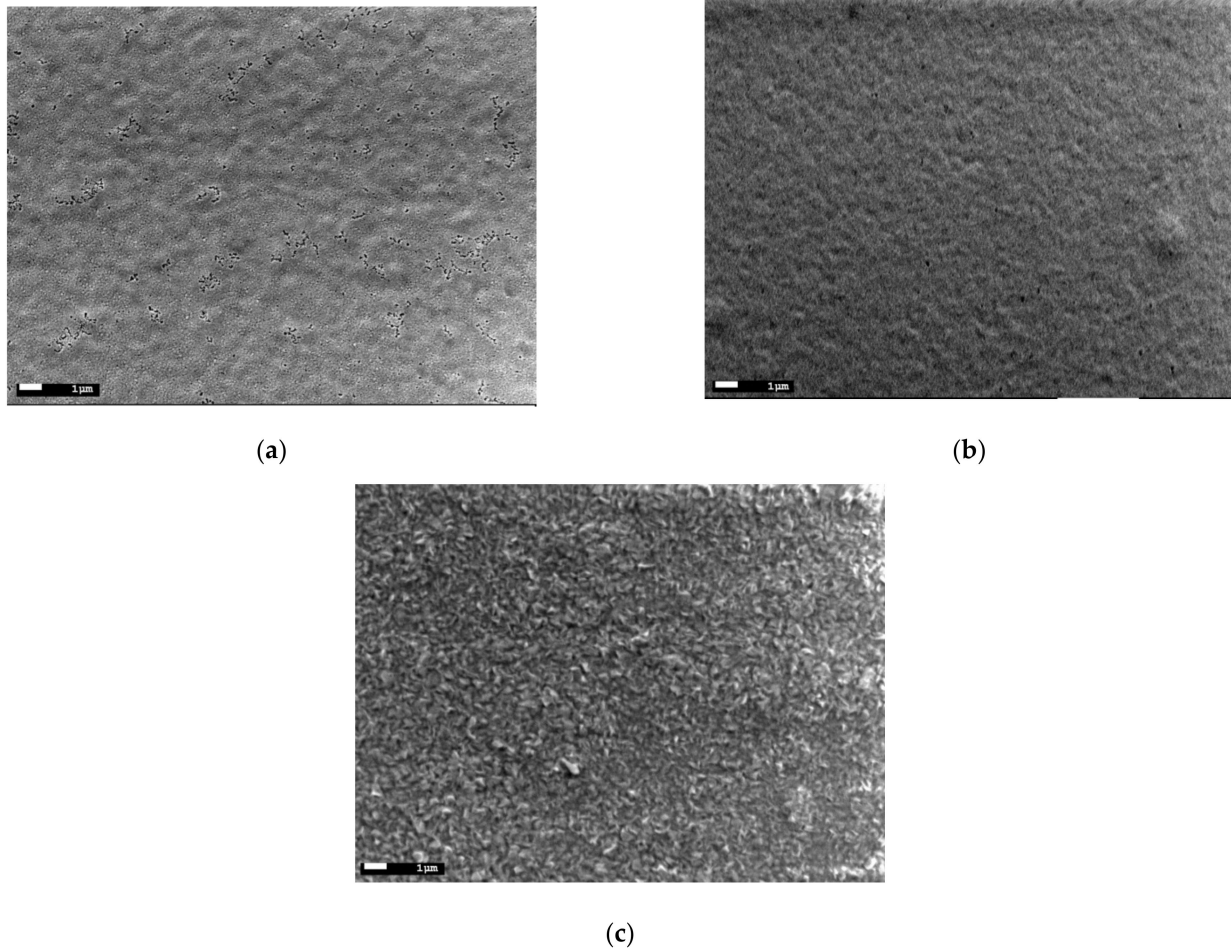


Figure 5. SEM images of the Bi_{1-x}Ba_xFeO₃ thin films for: x = 0 (a), x = 0.02 (b), and x = 0.05 (c).

3.2. Optical Properties of BBFO Thin Films

The optical properties of the studied BBFO films were investigated by recording their UV-vis absorption spectra which are shown in the Figure 6. The optical absorption provides important information about the electronic states of the systems since the UV-vis absorption edge is in strong correlation with the band gap energy of the photocatalyst [44,45].

It can be observed from Figure 6a that there is absorption in the range of about 400–550 nm, which indicates that all BiFeO₃-based films can absorb higher amounts of visible light. The optical measurements results suggest the potential applications of the Ba-doped BiFeO₃ films as visible-light photocatalysts. To estimate the energy band gap of the films, the Tauc formula [44] was used, given by the Equation (3):

$$\alpha h\nu = A(h\nu - E_g)^{n/2} \quad (3)$$

where α , h , ν , E_g , A , and n represent the absorption coefficient, Planck constant, light frequency, band gap energy, proportional constant, and the power index that depend on the nature of transition. The value of n is 1 if considering that BiFeO₃ is a direct band gap transition material [44]. The corresponding values of the E_g of BBFO films were estimated by extrapolating the linear part of the Tauc plots up to the $(\alpha h\nu)^2 = 0$ axis, as shown in

the Figure 6b. According to Tauc relation, the estimated values for the energy band gap are 2.3 eV, 2.2 eV, and 2.1 eV for $x = 0, 0.02,$ and 0.05 Ba doping concentrations. The band gap estimated for BFO of ~ 2.3 eV is comparable with the values reported in the literature for BiFeO₃-based systems [44,46,47]. Inset of the Figure 6b shows that the band gap is narrowed after doping with Ba ions and decreases gradually with the increase in the doping content, which is expected to result in an increase of photocatalytic response.

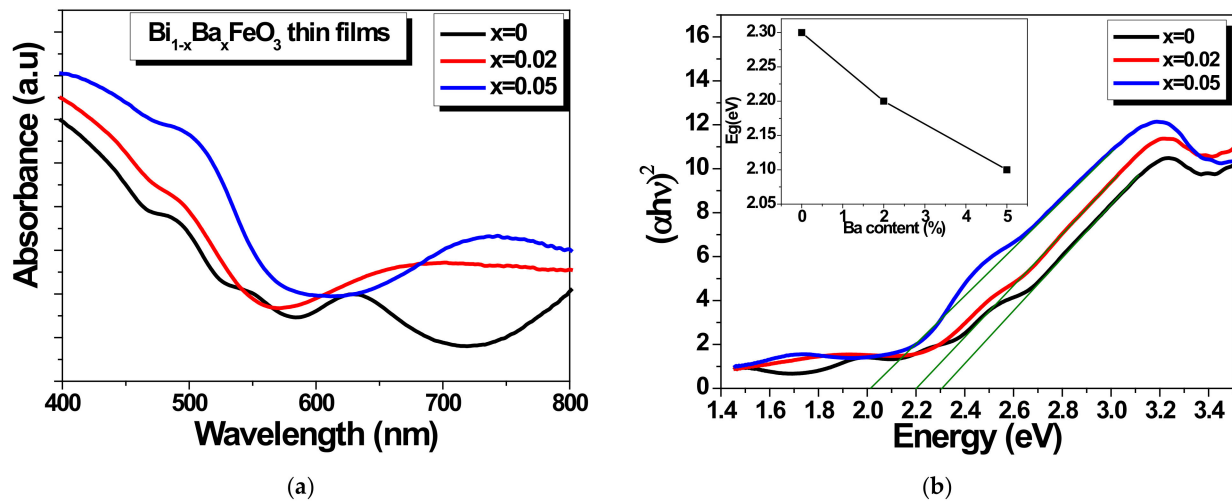


Figure 6. BBFO films optical properties: UV-vis absorption spectra (a). The calculation of the band gap energy of the BBFO films. Inset represents the band gap energy function of Ba concentration dependences (b).

3.3. Photocatalytic Degradation of RhB

The photocatalytic degradation ability of the BBFO films was tested using RhB as an organic pollutant for degradation. The tests of BBFO films as photocatalysts were carried out by exposing the films to solar light for 6 h. The corresponding absorption spectra were recorded in the range of (350–600) nm. For comparison, a reference absorption test in the dark was registered before each experiment. The aqueous solution was chosen to have the pH value of ~ 7 .

Figure 7 shows the UV-vis absorbance curves of RhB during photocatalytic degradation.

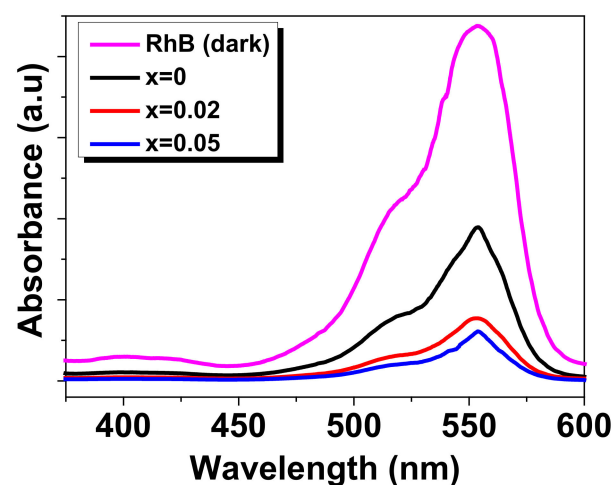


Figure 7. UV-vis absorbance spectra of photodegradation of the RhB solutions with BBFO thin films under solar light irradiation of 6 h.

It can be seen that Ba doping generally leads to a decrease of the absorbance of RhB in comparison to the non-irradiated reference demonstrating the photocatalytic activity of the studied films. As the concentration of Ba ions increases, the absorbance peak of the RhB degradation further decreases. The degradation efficiency (D) of RhB was determined using the following formula:

$$D(\%) = \frac{A_0 - A}{A_0} \times 100 \quad (4)$$

where A_0 represents the initial absorbance of RhB solution measured at $\lambda_{max} = 553$ nm and A is the absorbance after 6 h of solar light irradiation.

According to Figure 7, the calculated values for degradation efficiency for Ba-doped BFO thin films are: ~57% for $x = 0$, ~83% for $x = 0.02$, and ~86% for $x = 0.05$. It is obvious that the photocatalytic efficiency of BFO material was improved in the presence of Ba^{2+} ions for degradation of RhB. The higher degradation rate was obtained for the thin films with $x = 0.05$ Ba doping concentration since this film exhibits also the narrow band gap (2.1 eV) which results in the most efficient utilization of the sun light. It is known that the basic principle of semiconductor photocatalysis involves photogenerated electron-holes (e^- - h^+) pairs which react with the surface adsorbed oxygen or with water molecules to give reactive radicals leading to the decomposition of used pollutant [44,48]. The sunlight irradiation begins the photocatalytic reaction by absorbing the light ($h\nu$) energy which leads to the e^- - h^+ pairs generation that contributed to the formation of reactive radicals: (i) The e^- will react with the surface-adsorbed oxygen to generate superoxide radicals (O_2^-); (ii) the h^+ will react with water molecules to generate hydroxyl radicals (OH) [48]. Then, both hydroxyl radicals and superoxide play an important role in the degradation process of RhB. The present results can be explained by the fact that Ba doping leads to reducing of the recombination rate of photogenerated e^- - h^+ pairs (a better charge separation) which contribute to the formation of reactive radicals (their number increases with Ba addition increasing) and finally to the improving of photocatalytic response.

4. Conclusions

In the present work, it was investigated the influence of Ba doping on the structural, microstructural, optical properties, and photocatalytic activity of BFO thin films. $Bi_{1-x}Ba_xFeO_3$ thin films were synthesized on glass substrates by using sol-gel-assisted spin-coating technique. The X-ray analysis revealed the formation of rhombohedral perovskite structure for all deposited films. FTIR results confirm that the BBFO have crystallized in a perovskite structure due to the presence of metal-oxide bands in the measured spectrum. The AFM morphology images evidenced an increase in the surface root mean square roughness with increasing percentage of Ba^{2+} ions from 4.9 nm for the pure BFO to 8.9 nm and 31.8 nm for $x = 0.02$ and $x = 0.05$ Ba doping concentrations, respectively. The optical measurements results suggest the potential applications of the Ba-doped $BiFeO_3$ films as visible-light photocatalysts due to the narrowing of the band gap after the doping with Ba ions which decreases gradually with the increase in the doping content. The photocatalytic tests revealed that Ba doping of BFO material leads to the enhancement of photocatalytic response. Therefore, Ba-doped $BiFeO_3$ thin films are good candidates for applications as visible-light photocatalysts.

Author Contributions: Conceptualization, F.G.; methodology, K.A. and B.A.; investigation, K.A. and B.A.; resources, K.A. and B.A.; data curation, K.A. and B.A.; writing—original draft preparation, F.G.; writing—review and editing, F.G. All authors have read and agreed to the published version of the manuscript.

Funding: Romanian Ministry of Research, Innovation and Digitization, Program 1-Development of the national R&D system, Subprogram 1.2—Institutional performance—RDI excellence financing projects: Contract no.11PFE/30.12.2021.

Acknowledgments: Authors are thankful to Romanian Ministry of Research, Innovation and Digitization, Program 1-Development of the national R&D system, Subprogram 1.2—Institutional performance—RDI excellence financing projects, Contract no.11PFE/30.12.2021, for financial support.

Conflicts of Interest: The authors declare no conflict of interest.

References

1. Ameta, R.; Benjamin, S.; Ameta, A.; Ameta, S.C. Photocatalytic Degradation of Organic Pollutants: A Review. *Mater. Sci. Forum* **2013**, *734*, 247–272. [[CrossRef](#)]
2. Chen, D.; Cheng, Y.; Zhou, N.; Chen, P.; Wang, Y.; Li, K.; Hua, S.; Cheng, P.; Peng, P.; Zhang, R.; et al. Photocatalytic degradation of organic pollutants using TiO₂-based photocatalysts: A review. *J. Clean. Prod.* **2020**, *268*, 121725. [[CrossRef](#)]
3. Di Mauro, A.; Fragalà, M.E.; Privitera, V.; Impellizzeri, G. ZnO for application in photocatalysis: From thin films to nanostructures. *Mater. Sci. Semicond. Process.* **2017**, *69*, 44–51. [[CrossRef](#)]
4. Hitam, C.N.C.; Jalil, A.A. A review on exploration of Fe₂O₃ photocatalyst towards degradation of dyes and organic contaminants. *J. Environ. Manage.* **2020**, *258*, 110050. [[CrossRef](#)]
5. Cheng, L.; Xiang, Q.; Liao, Y.; Zhang, H. CdS-based photocatalysts. *Energy Environ. Sci.* **2018**, *11*, 1362–1391. [[CrossRef](#)]
6. Lee, G.-J.; Wu, J.J. Recent developments in ZnS photocatalysts from synthesis to photocatalytic applications—A review. *Powder Technol.* **2017**, *318*, 8–22. [[CrossRef](#)]
7. Haider, A.J.; Jameel, Z.N.; Al-Hussaini, I.H.M. Review on: Titanium Dioxide Applications. *Energy Procedia* **2019**, *157*, 17–29. [[CrossRef](#)]
8. Zoubi, W.A.; Al-Hamdani, A.A.S.; Sunghun, B.; Ko, Y.G. A review on TiO₂-based composites for superior photocatalytic activity. *Rev. Inorg. Chem.* **2021**, *41*, 213–222. [[CrossRef](#)]
9. Mushtaq, F.; Chen, X.; Torlakcik, H.; Nelson, B.J.; Panè, S. Enhanced catalytic degradation of organic pollutants by multi-stimuli activated multiferroic nanoarchitectures. *Nano Res.* **2020**, *13*, 2183–2191. [[CrossRef](#)]
10. Mettout, B.; Toledano, P. Theory of the photovoltaic and light-induced effects in multiferroics. In *Emerging Photovoltaic Materials (Silicon & Beyond)*; ch. 7. part II.; Kurinec, S.K., Ed.; John Wiley&Sons: Hoboken, NJ, USA, 2018; pp. 195–238.
11. Ianculescu, A.; Prihor, F.; Postolache, P.; Mitoseriu, L.; Dragan, N.; Crisan, D. Preparation, Structural and Magnetic Properties of Mn-Doped La_{0.1}Bi_{0.9}FeO₃ Ceramics. *Ferroelectrics* **2009**, *391*, 67–75. [[CrossRef](#)]
12. Gheorghiu, F.; Curecheriu, L.; Ianculescu, A.; Calugaru, M.; Mitoseriu, L. Tunable dielectric characteristics of Mn-doped BiFeO₃ multiferroic ceramics. *Scr. Mater.* **2013**, *68*, 305–308. [[CrossRef](#)]
13. Gheorghiu, F.; Tanasa, R.; Buscaglia, M.T.; Buscaglia, V.; Pastravanu, C.G.; Popovici, E.; Mitoseriu, L. Preparation of Bi₂Fe₄O₉ particles by hydrothermal synthesis and functional properties. *Phase Transit.* **2013**, *86*, 726–736. [[CrossRef](#)]
14. Tuluk, A.Y.; Mahon, T.R.; van der Zwaag, S.; Groen, P. BiFeO₃ synthesis by conventional solid-state reaction. In Proceedings of the 2019 IEEE International Symposium on Applications of Ferroelectrics (ISAF), Lausanne, Switzerland, 14–19 July 2019; pp. 1–4. [[CrossRef](#)]
15. Han, S.H.; Kim, K.S.; Kim, H.G.; Lee, H.-G.; Kang, H.-W.; Kim, J.S.; Cheon, C.I. Synthesis and characterization of multiferroic BiFeO₃ powders fabricated by hydrothermal method. *Ceram. Int.* **2010**, *36*, 1365–1372. [[CrossRef](#)]
16. Majid, F.; Mirza, S.T.; Riaz, S.; Naseem, S. Sol-Gel Synthesis of BiFeO₃ Nanoparticles, *Mater. Today Proc.* **2015**, *2*, 5293–5297.
17. Penalva, J.; Lazo, A. Synthesis of Bismuth Ferrite BiFeO₃ by solution combustion method. *J. Phys. Conf. Ser.* **2018**, *1143*, 12025. [[CrossRef](#)]
18. Ferri, E.A.V.; Santos, I.A.; Radovanovic, E.; Bonzanini, R.; Giroto, E.M. Chemical Characterization of BiFeO₃ Obtained by Pechini Method. *J. Braz. Chem. Soc.* **2008**, *19*, 1153–1157. [[CrossRef](#)]
19. Reddy, V.R.; Kothari, D.; Upadhyay, S.K.; Gupta, A.; Chauhan, N.; Awasthi, A.M. Reduced leakage current of multiferroic BiFeO₃ ceramics with microwave synthesis. *Ceram. Int.* **2014**, *40*, 4247–4250. [[CrossRef](#)]
20. Gheorghiu, F.P.; Ianculescu, A.; Postolache, P.; Lupu, N.; Dobromir, M.; Luca, D.; Mitoseriu, L. Preparation and properties of (1-x)BiFeO₃-xBaTiO₃ multiferroic ceramics. *J. Alloy. Compd.* **2010**, *506*, 862–867. [[CrossRef](#)]
21. Zargazi, M.; Entezari, M.H. A novel synthesis of forest like BiFeO₃ thin film: Photo-electrochemical studies and its application as a photocatalyst for phenol degradation. *Appl. Surf. Sci.* **2019**, *483*, 793–802. [[CrossRef](#)]
22. Li, P.; Lin, Y.-H.; Nan, C.W. Effect of nonmagnetic alkaline-earth dopants on magnetic properties of BiFeO₃ thin films. *J. Appl. Phys.* **2011**, *110*, 033922. [[CrossRef](#)]
23. Gaur, A.; Singh, P.; Choudhary, N.; Kumar, D.; Shariq, M.; Singh, K.; Kaur, N.; Kaur, D. Structural, optical and magnetic properties of Nd-doped BiFeO₃ thin films prepared by pulsed laser deposition. *Phys. B Condens. Matter* **2011**, *406*, 1877–1882. [[CrossRef](#)]
24. Wang, H.; Huang, J.; Xing, S.; Jian, J.; Liu, J.; Wang, H. Effective doping control in Sm-doped BiFeO₃ thin films via deposition temperature. *RSC Adv.* **2020**, *10*, 40229–40233. [[CrossRef](#)]
25. Hu, B.L.; Li, Z.Z.; Zhang, H.Q.; Chen, S.Y.; Ye, Q.Y.; Zhao, J.F.; Zhao, Y.; Huang, Z.G. Preparation and Properties of La-Doped BiFeO₃ Thin Films. *Mater. Sci. Forum.* **2016**, *848*, 645–651. [[CrossRef](#)]
26. Soltani, T.; Lee, B.-K. Novel and facile synthesis of Ba-doped BiFeO₃ nanoparticles and enhancement of their magnetic and photocatalytic activities for complete degradation of benzene in aqueous solution. *J. Hazard. Mater.* **2016**, *316*, 122–133. [[CrossRef](#)]

27. Feng, Y.N.; Wang, H.C.; Shen, Y.; Lin, Y.H.; Nan, C.W. Magnetic and Photocatalytic Behaviors of Ba-Doped BiFeO₃ Nanofibers. *Int. J. Appl. Ceram. Technol.* **2014**, *11*, 676–680. [[CrossRef](#)]
28. Mahbub, R.; Islam, M.F. Sintering Behavior and Microstructure Development of Ba Doped BiFeO₃. *Int. J. Innov. Technol. Explor. Eng.* **2014**, *3*, 2278.
29. Shah, S.M.H.; Riaz, S.; Hussain, S.S.; Atiq, S.; Naseem, S. Structural, Magnetic and Dielectric Properties of Ba Doped BiFeO₃ Thin Films. *Mater. Today Proc.* **2015**, *2*, 5654–5659. [[CrossRef](#)]
30. Pani, T.K.; Sundaray, B.; Sahoo, G.; Rout, D. Influence of Barium Doping on Structural and Magnetic Properties of Bismuth Ferrite Thin Films via Spray Pyrolysis Method. *J. Phys. D Appl. Phys.* **2020**, *53*, 325001. [[CrossRef](#)]
31. Patterson, A.L. The Scherrer Formula for X-Ray Particle Size Determination. *Phys. Rev.* **1939**, *56*, 978–982. [[CrossRef](#)]
32. Shannon, R.D. Revised effective ionic radii and systematic studies of interatomic distances in halides and chalcogenides. *Acta Cryst.* **1976**, *A32*, 751–767. [[CrossRef](#)]
33. Li, Z.; Yang, M.; Park, J.S.; Wei, S.H.; Berry, J.J.; Zhu, K. Stabilizing perovskite structures by tuning tolerance factor: Formation of formamidinium and cesium lead iodide solid-state alloys. *Chem. Mater.* **2016**, *28*, 284–292. [[CrossRef](#)]
34. Suryanarayana, C.; Norton, M.G. *X-ray Diffraction: A Practical Approach*; Springer Science & Business Media: Berlin/Heidelberg, Germany, 1998.
35. Cebela, M.; Jankovic, B.; Hercigonja, R.; Lukic, M.J. Comprehensive characterization of BiFeO₃ powder synthesized by the hydrothermal procedure. *Process. Appl. Ceram.* **2016**, *10*, 201–208. [[CrossRef](#)]
36. Anthonyraj, C.; Muneeswaran, M.; Raj, S.G.; Giridharan, N.V.; Sivakumar, V.; Senguttuvan, G. Effect of samarium doping on the structural, optical and magnetic properties of sol-gel processed BiFeO₃ thin films. *J. Mater. Sci. Mater. Electron.* **2015**, *26*, 49–58. [[CrossRef](#)]
37. Mishra, R.K.; Pradhan, D.K.; Choudhary, R.N.P.; Banerjee, A. Effect of yttrium on improvement of dielectric properties and magnetic switching behavior in BiFeO₃. *J. Phys. Condens. Matter.* **2008**, *20*, 45218. [[CrossRef](#)]
38. Yongming, H.; Fei, L.; Zhang, Y.; Yuan, J.; Wang, Y.; Gu, H. Synthesis of bismuth ferrite nanoparticles via a wet chemical route at low temperature. *J. Nanomater.* **2011**, *2011*, 6. [[CrossRef](#)]
39. Mevada, K.C.; Patel, V.D.; Patel, K.R. FT-IR, XRD and thermal studies of gel-grown barium tartrate crystals. *Arch. Phys. Res.* **2012**, *3*, 258–263.
40. Vijayasundaram, S.V.; Kanagadurai, R. Size dependent magnetic properties of BiFeO₃ nanoparticles: A multifunctional material for saving energy. *Int. J. ChemTech Res.* **2015**, *8*, 436–440.
41. Hojamberdiev, M.; Xu, Y.; Wang, F.; Liu, W.; Wang, J. La-modification of multiferroic BiFeO₃ by hydrothermal method at low temperature. *Inorg. Mater.* **2009**, *45*, 1183–1187. [[CrossRef](#)]
42. Ma, Y.; Chen, X.M. Enhanced multiferroic characteristics in NaNbO₃-modified BiFeO₃ ceramics. *J. Appl. Phys.* **2009**, *105*, 054107–054115. [[CrossRef](#)]
43. Chaudhuri, A.; Mandal, K. Study of structural, ferromagnetic and ferroelectric properties of nanostructured barium doped bismuth ferrite. *J. Magn. Magn. Mater.* **2014**, *353*, 57–64. [[CrossRef](#)]
44. Xu, X.; Lin, Y.H.; Li, P.; Shu, L.; Nan, C.W. Synthesis and photocatalytic behaviors of high surface area BiFeO₃ thin films. *J. Am. Ceram. Soc.* **2011**, *94*, 2296–2299. [[CrossRef](#)]
45. Soltani, T.; Entezari, M.H. Sono-synthesis of bismuth ferrite nanoparticles with high photocatalytic activity in degradation of Rhodamine B under solar light irradiation. *Chem. Eng. J.* **2013**, *223*, 145–154. [[CrossRef](#)]
46. Sharma, S.; Kumar, M. Band gap tuning and optical properties of BiFeO₃ nanoparticles. *Mater. Today Proc.* **2020**, *28*, 168–171. [[CrossRef](#)]
47. Zhang, Y.; Yang, Y.; Dong, Z.; Shen, J.; Song, Q.; Wang, X.; Mao, W.; Pu, Y.; Li, X. Enhanced photocatalytic activity of Ba doped BiFeO₃ by tuning morphology and band gap. *J. Mater. Sci. Mater. Electron.* **2020**, *31*, 15007–15012. [[CrossRef](#)]
48. Haruna, A.; Abdulkadir, I.; Idris, S.O. Photocatalytic activity and doping effects of BiFeO₃ nanoparticles in model organic dyes. *Heliyon* **2020**, *6*, e03237. [[CrossRef](#)] [[PubMed](#)]